Nanoscale Horizons

ROYAL SOCIETY OF CHEMISTRY

COMMUNICATION

View Article Online
View Journal | View Issue

Cite this: *Nanoscale Horiz.*, 2024, **9**, 1354

Received 29th March 2024,
Accepted 3rd June 2024

DOI: 10.1039/d4nh00136b

rsc.li/nanoscale-horizons

Bionic dual-scale structured films for efficient passive radiative cooling accompanied by robust durability†

Renwei Zhang, Ningning Sun, Zehong Zhao, Shixu Wang, Mengfan Zhang, Lei Zhao, Yahua Liu and Shile Feng *

Passive radiative cooling (PRC), as an energy-free cooling approach, is ingeniously harnessed for certain natural organisms to withstand extreme high-temperature climates, which has inspired numerous bionic designs. However, it is a great challenge to enhance the durability of the designed materials in practical scenarios while inheriting the natural biological principles. We demonstrate bionic dual-scale structured (BDSS) films for efficient passive radiative cooling accompanied by robust durability after discovering the excellent thermoregulatory properties of the inner surface of Hawaiian scallop shell. We found that the inner surface of the shell consists of large-scale triangular ridges scattered with small-scale terrace steps. This dual-scale structure can enhance the reflectivity of sunlight by efficient Mie scattering and increase the emissivity in the mid-infrared range by lengthening the propagation of photons, thereby decreasing the surface temperature. Underpinned by this finding, we developed a BDSS film that features a strong solar spectrum reflectivity of 0.95 and a high mid-infrared emissivity of 0.98, achieving a sub-ambient cooling of 10.8 °C under direct sunlight. Additionally, the designed films possess robust durability including excellent self-cleaning, flexibility, mechanical strength, chemical stability, and anti-ultraviolet radiation, which is promising for thermal thermoregulation in various harsh scenarios.

New concepts

Various natural organisms have evolved special structures for passive radiative cooling to withstand extreme high-temperature climates, which has motivated bionic enthusiasm. Despite great progress, enhancing the durability of designed materials for use in practical scenarios is still challenging. Here, we have for the first time discovered the excellent passive radiative cooling capacity of the inner surface of *Hawaiian scallop* shells underpinned by the dual-scale structure, and proposed an ingenious method for bionic design and fabrication. Based on the enhanced effect of the dual-scale structure on the solar spectrum reflectivity and mid-infrared emissivity, respectively, the bionic films exhibit an efficient passive radiative cooling performance with a sub-ambient cooling of 10.8 °C under direct sunlight. Moreover, the designed film accompanied by robust durability endowed with excellent self-cleaning, flexibility, mechanical strength, chemical stability, and anti-ultraviolet radiation, is promising for thermal thermoregulation in a sustainable and energy-free manner.

Introduction

As climate change and global warming intensify, humanity faces an ever-increasing demand for cooling electricity.[1] Certain conventional cooling devices, including fans and air conditioners, not only require an enormous quantity of energy but also emit a considerable amount of greenhouse gases.[2,3] In contrast, passive radiative cooling (PRC) has become a promising technique,[4–8] which can lower the surface temperature of a directly sky-facing object by efficiently reflecting sunlight in the solar spectrum band (0.25–2.5 μm)[9–14] and perpetually dissipating excessive heat to the cryogenic universe through an atmospheric transparent window (8–13 μm) with no energy consumption.[15–21]

Previously, numerous radiative cooling systems have been proposed by designing structures in subwavelength-scale dimensions.[22–27] For example, Fan *et al.*[28] built a PRC system consisting of an interactive stack of HfO_2 and SiO_2 layered over a silver reflecting layer, which achieved a cooling of 4.9 °C below ambient temperature. Zou *et al.*[29] designed a metal-loaded dielectric resonator surface with silver plating on the doped silicon surface to achieve high mid-infrared emissivity. However, limited by the existing knowledge and experiences, the design of PRC materials is still facing severe bottlenecks, especially reflected in poor cost-effectiveness, environmental stability and lack of spectral selectivity.[30–33]

To address the above bottlenecks, many researchers are looking to nature for inspiration. Amazing discoveries show that some natural organisms have evolved special structures for

State Key Laboratory of High-performance Precision Manufacturing, Dalian University of Technology, Dalian 116024, P. R. China.
E-mail: fengshile@dlut.edu.cn

† Electronic supplementary information (ESI) available: Experimental section. Fig. S1–S13. Video S1. See DOI: https://doi.org/10.1039/d4nh00136b

PRC to withstand extreme high-temperature climates, which are mainly underpinned by structural whiteness or silver color.[15,34–41] For instance, *Silver Saharan* ants, surviving in the scorching desert, manifest strong thermoregulation attributed to their triangular-hair induced efficient solar spectrum reflectivity and mid-infrared emissivity.[42] The white *Goliathus* beetle has a gorgeous hollow cylinder or shell structure that allows for radiative heat dissipation and broadband reflectivity.[43] The comet moth, *Argema mittrei*, shows a broadband high reflectivity based on the strong scattering of sunlight that is induced by the filamentary air voids.[44] All these findings motivated a bionic enthusiasm for PRC. Despite great processes, the biomimetic structures are usually porous structures, which bring defects in mechanical strength.[45] It is challenging to enhance the durability of designed materials in practical scenarios.

The *Hawaiian scallop* is a shallow sea mollusk with an unmistakably white inner surface. In addition, the *Hawaiian scallop* will face challenges of survival in extremely high temperature conditions when stranded on the beach. Therefore, we suspected that it had radiative cooling properties and carried out further measurements. According to a cooling test at noon in Dalian, the inner surface of the shell manifests an average cooling of ~4 °C, showing an excellent cooling performance (Fig. S1, ESI†). This result is attributed to the dual-scale structure of the inner surface of Hawaiian scallop shell consisting of large-scale (~10 μm) triangular ridges scattered with small-scale (~1 μm) terrace steps, which enhances the reflectivity of sunlight by efficient Mie scattering and increases the mid-infrared emissivity by lengthening the propagation of photons. By imitating this, we constructed bionic dual-scale structural (BDSS) films by Al_2O_3 particle doping and poly (dimethylsiloxane) (PDMS) molding methods. Sub-ambient cooling of 10.8 °C under direct sunlight on the designed film is endowed by a strong solar spectrum reflectivity of 0.95 and a high mid-infrared emissivity of 0.98, respectively. The BDSS film also possesses outstanding self-cleaning, anti-corrosion of acid and alkali, flexibility, mechanical strength, and anti-UV radiation performances, which enhances the durability of the designed films for applications in various harsh outdoor environments.

Results and discussion

Morphology and optical properties of the inner surface of the shell

The inner surface of a *Hawaiian scallop* shell exhibits a bright white color and possesses radially diverging stripes, indicating the existence of strong light reflectivity and specific morphology (Fig. 1a). Further scanning electron microscopy (SEM) images show that the target surface manifests a dual-scale structure that consists of larger-scale triangular ridges (~10 μm) scattered with quasi-parallel terrace steps (~1 μm), as shown in Fig. 1b and c. To verify the effect of the dual-scale structure on the optical properties, we examined the reflectivity in the solar spectrum and the emissivity in the mid-infrared region of the inner surface of a *Hawaiian scallop* shell with and without dual-scale structures (Fig. 1d and e). Here the inner surface of the Hawaiian scallop shell without a dual-scale structure was obtained by grinding the target surface as flat as possible using a small electric grinder, as shown in Fig. S2 (ESI†). We find that the solar spectrum reflectivity and the mid-infrared emissivity of the inner surface of Hawaiian scallops are 0.6339 and 0.9497, respectively, which are both higher than those of surfaces without dual-scale structure. This result demonstrates that the dual-scale structure can enhance both the solar spectrum reflectivity and the mid-infrared emissivity, which achieves a cooling of ~4.9 °C below ambient temperature (Fig. S2, ESI†).

To further explore the mechanism for the dual-scale structural effect on solar spectrum reflectivity, finite-difference time-domain (FDTD) simulation was employed. By importing the structural and optical characteristic parameters into FDTD, the modes of photon dynamics on dual-scale, single large-scale, and single small-scale structures were established (Fig. 1f). Here the optical characteristic parameters are refractive index n and extinction coefficient k with values shown in Fig. S3 (ESI†), which are measured using a spectroscopic ellipsometer. In the modes, the red area represents a higher electromagnetic field as well as a higher Mie scattering of photons. We find that the dual-scale structure and the single small-scale structure manifest a more intense Mie scattering in contrast to that for the single large-scale structure, which is due to the existence of numerous small-scale steps (~1 μm) with size comparable to the wavelength of the solar spectrum (~0.25–2.5 μm). This efficient Mie scattering further enhances the solar spectrum reflectivity. This result further illustrates that the solar spectrum reflectivity is mainly affected by the small-scale structure. In addition, the interference and diffraction effects of light work together on the reflection of sunlight, increasing the overall solar reflectivity.

The enhanced effect of the dual-scale structure on mid-infrared emissivity is because the larger-scale triangular structure (~10 μm) displays a similar size to the wavelength of mid-infrared wavelengths (~8–13 μm). This matching of the scales prevents photons from directly passing through the surface, causing them to continue to oscillate between the structures. This unique photon dynamic increases the propagation path of light and thus enhances the absorption rate in the corresponding band.[46] At the same time, the staggered arrangement of small-scale structures (~1 μm) at the edges of large-scale structures results in different refractive indexes in the mid-infrared band at different locations, which will lead to an increase in the absorption rate after light is incident. Therefore, the absorption rate increases after light is incident. Based on Kirchhoff's law, the absorption rate is equal to the emissivity.[41] Therefore, the mid-infrared emissivity is improved by the dual-scale structure.

Design and preparation of BDSS films

The dual-scale structure of the inner surface of the Hawaiian *scallop* shell possesses two typical structural features, *i.e.*, large-

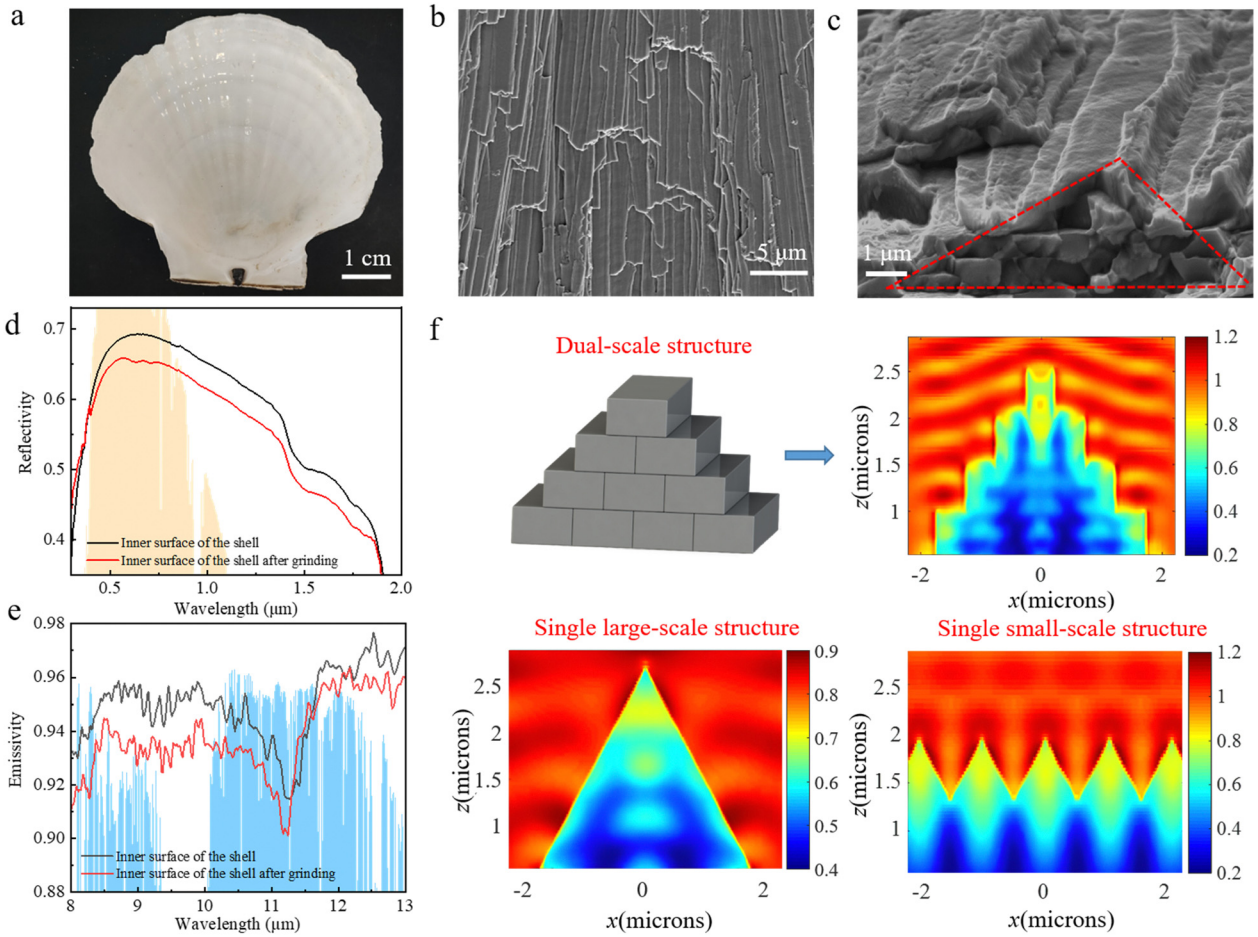

Fig. 1 The morphology and optical properties of the inner surface of the *Hawaiian scallop* shell. (a) Optical photograph of the inner surface of the *Hawaiian scallop* shell. (b) SEM image of the inner surface of the *Hawaiian scallop* shell. (c) The enlarged SEM image of the cross-section of the inner surface. (d) Comparison of reflectivity in the solar spectrum band of a *Hawaiian scallop* shell before and after grinding. (e) Comparison of emissivity in the atmospheric window bands (8–13 μm) of a *Hawaiian scallop* shell before and after grinding. (f) Modes of photon dynamics on dual-scale and single-scale structures.

scale triangular ridges and small-scale terrace steps (Fig. 1c). We propose a design strategy to construct a bionic dual-scale structure (BDSS) by particle doping and polymer molding methods (Fig. 2a). The template for polymer molding was fabricated *via* the photolithography technique on a silicon wafer, which consists of triangular ridges. The BDSS film was obtained by spinning a mixture of Al_2O_3 particles and PDMS in a certain proportion on the template, followed by subsequent curing and demolding processes (Fig. 2b, details shown in the experimental section). The thickness (t) of the film can be tuned by the rotational speed of the spin-coating. Here, the triangular ridges of the template manifest a base angle α of 55° and space d of 6, 8, 10, and 12 μm (Fig. 2c and Fig. S4, ESI†). The mass ratio r of Al_2O_3 to PDMS changes from 6 : 10 to 14 : 10 and the Al_2O_3 particles possess multi-angular and irregular shapes with sizes s of 0.1 and 1 μm (Fig. S5, ESI†). Fig. 2d shows that the fabricated film manifests an ultra-white appearance with a mass ratio r of PDMS to Al_2O_3 (size of ~1 μm) at 12 : 10. More microscopic observation shows that Al_2O_3 particles are stacked to form a dual-scale structure with larger-scale triangular ridges and small-scale edges encapsulated in PDMS ridges (Fig. S6, ESI†). Note here that both the larger-scale triangular ridges and small-scale edges for the dual-scale structures are formed by the stacking of Al_2O_3 particles. The PDMS with triangular ridges only acts as a supporting skeleton. Based on the extreme transparency of PDMS,[41] the photons can interact well with the dual-scale structure, which leads to strong sunlight scattering as well as ultra-white appearance of the designed films.

We further investigated the effect of the mass ratio r of Al_2O_3 to PDMS, the Al_2O_3 particle size s, the triangular ridge space d, and the film thickness t on the optical properties of the designed films including the reflectivity in the solar spectrum and the emissivity in the mid-infrared region, as shown in Fig. 3a–c and Fig. S7 (ESI†). The results indicate that the solar spectrum reflectivity is mainly influenced by the mass ratio r of Al_2O_3 to PDMS, the Al_2O_3 particle size s, and film thickness t, while the mid-infrared emissivity is mainly influenced by the triangular ridge space d. This result is because light mainly interacts with structures corresponding to its wavelength.

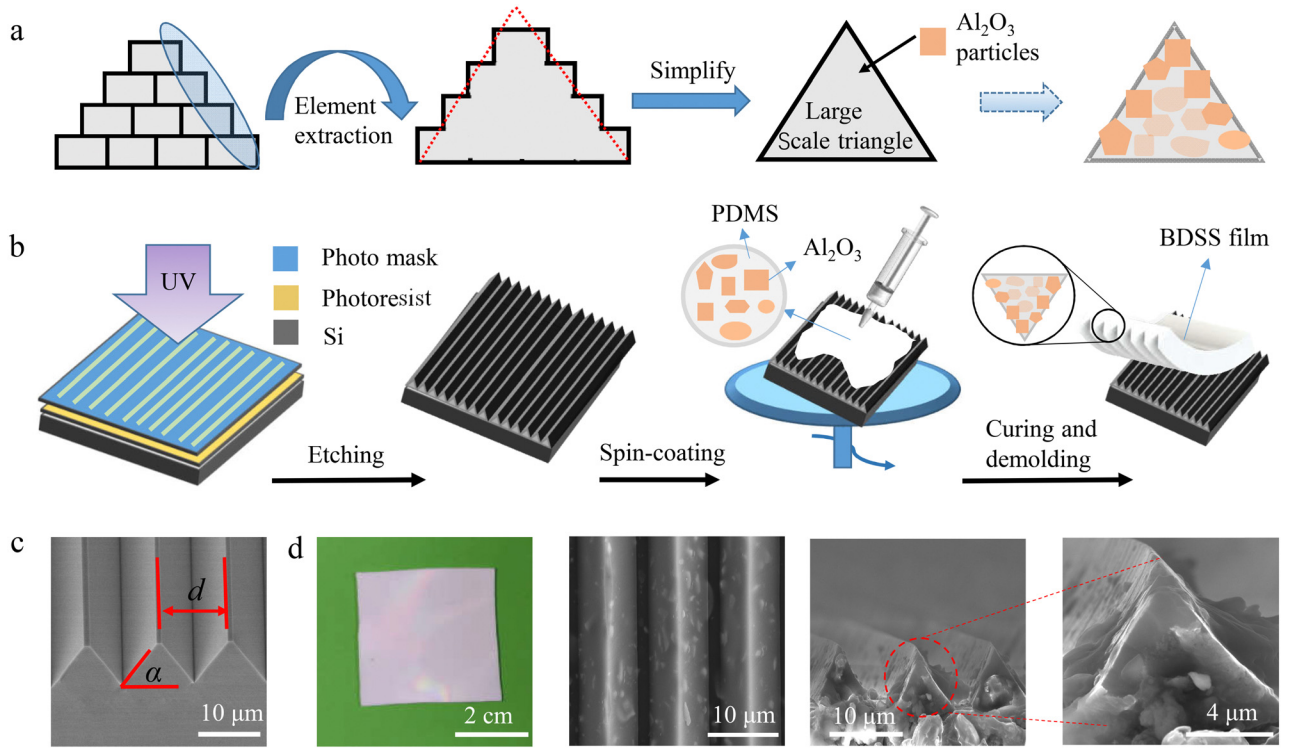

Fig. 2 Design and preparation of the BDSS films. (a) The characteristic model extracted from the microstructure of the inner surface of the *Hawaiian scallop* shell. (b) The schematic diagram of the particle doping and polymer molding processes. (c) The SEM image of the silicon wafer template. (d) The optical and SEM images of the BDSS film.

When the mass ratio r of Al_2O_3 to PDMS increases, the mid-infrared emissivity is relatively stable, while the solar spectrum reflectivity increases first and then decreases, reaching a peak value of 0.76 at r of 12 : 10 (Fig. 3a). This is because the number of Al_2O_3 particles with size compared to the solar spectrum (0.25–5 μm) is the major factor in determining the solar spectrum reflectivity. However, too high content of Al_2O_3 particles causes them to agglomerate and form large-scale clumps, which reduces the reflectivity (Fig. S8, ESI†). Therefore, we chose a sample fabricated at the ratio of 12 : 10 for further experiments. Similar to Al_2O_3 particle content, the Al_2O_3 particle size also only influences the solar spectrum reflectivity of the designed film. For Al_2O_3 particles with average size changes from ∼0.1 to ∼1 μm, the solar spectrum reflectivity changes from 0.76 to 0.95 (Fig. 3b). The result is due to the Al_2O_3 particles having an average size of ∼1 μm with more particles located in the solar spectrum range (Fig. S5, ESI†). In addition, the film thickness t also mainly influences the solar spectrum reflectivity, exhibiting a positive correlation (Fig. S7, ESI†), attributed to an increase in the backscattering of light as thickness increases.[47] Since the solar spectrum reflectivity increases very little when the thickness exceeds 682 μm, we choose it as the optimal result for cost considerations.

In contrast to the above parameters, the triangular ridge space d mainly influences the mid-infrared emissivity of BDSS films, while affecting little the solar spectrum reflectivity, as shown in Fig. 3c. With d increasing from 6 to 12 μm, the highest mid-infrared emissivity of ∼0.98 appears at d of 6 and 8 μm and then decreases gradually. However, BDSS films with d of 6 μm not only manifest high emissivity in the mid-infrared range (8–13 μm), but also in the spectral band of 6–8 μm. According to Kirchhoff's law, the emissivity is equal to absorptivity. This means that the film absorbs additional heat at the spectral band of 6–8 μm (not the atmospheric transparent window, 8 ∼ 13 μm) without emitting it into outer space, which leads to a temperature rise. Therefore, the BDSS film with d of 8 μm is optimal for achieving high emissivity at the atmospheric window. Moreover, the mid-infrared emissivity can also be affected by the materials. PDMS and Al_2O_3 particles are promising materials for enhancing mid-infrared emissivity based on the elected molecular vibrations of PDMS and strong phonon polariton resonance of Al_2O_3, respectively.[41]

According to the above investigations, we obtain the optimal fabricating parameters for BDSS films as r of 12 : 10, s of 1 μm, t of 682 μm and d of 8 μm, respectively. Comparing the optical properties of the BDSS film with the optimal dual-scale structure and flat surface with the same materials, we obtain that the BDSS film exhibits a high solar spectrum reflectivity of 0.95 and mid-infrared emissivity of 0.98, which are 25% and 2% higher than those of the flat surfaces, as shown in Fig. 3d. This result demonstrates the enhanced effect of the dual-scale structure on both solar spectrum reflectivity and mid-infrared emissivity. It is worth highlighting that a range of PDMS-based films can be fabricated by implanting various ceramic particles, including

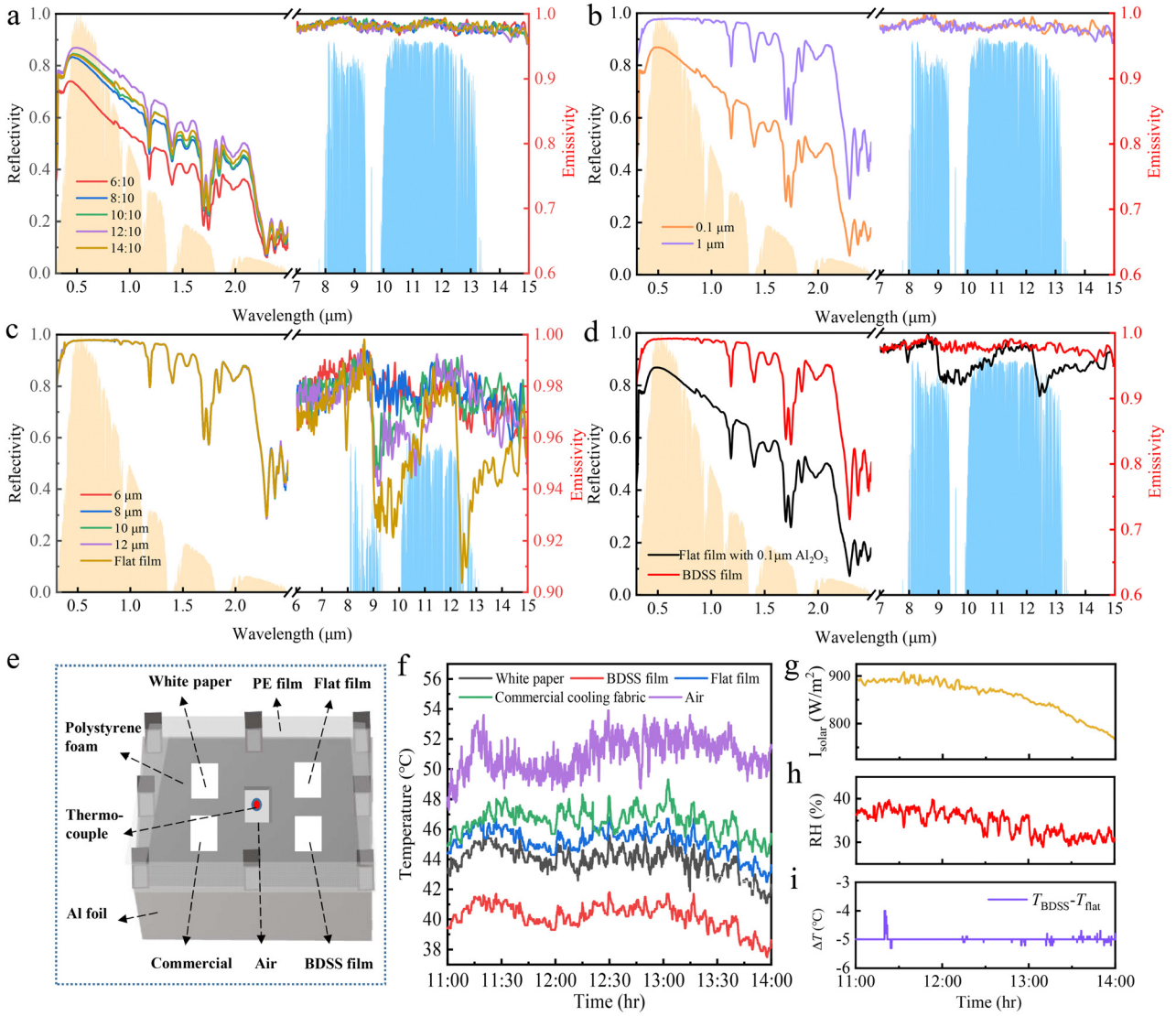

Fig. 3 Optical properties and PRC performance of the BDSS film. (a) The effect of the doping concentration of Al_2O_3 on the optical properties of the BDSS film. (b) The effect of the size of the Al_2O_3 particles on the optical properties of the BDSS film. (c) The effect of triangular ridge space on the optical properties of the BDSS film. (d) The optical properties of the BDSS film compared with those of the flat film with the same materials. (e) The internal structure diagram of the cooling measuring device. (f) Cooling curves of BDSS films, flat film, white paper, commercial cooling fabric, and air. (g) Solar power of the test site. (h) Humidity of the test site. (i) The temperature difference between the BDSS film and the flat film.

Y_2O_3, ZrO_2, SiO_2, and MgO, *etc.* The appearances, SEM images and optical properties of these films are presented in Fig. S9 and S10 (ESI†). All of these films have an ultra-white appearance, strong solar reflectivity, and mid-infrared emissivity. This result indicates that our approach provides a generic manner for bionic fabrication.

Outdoor passive radiative cooling performance of BDSS films

We implemented the outdoor radiative cooling capability of the BDSS films by using a self-made experimental setup (Fig. S11, ESI†) at Dalian, Liaoning Province, China (38°53′ N, 121°29′ E) on June 15, 2023, from 11 : 00 to 14 : 00. The experimental setup is constructed by polystyrene foam wrapped with high reflective aluminum foil to minimize the influence of environmental heat conduction and sealed with a transparent PE film without affecting the incidence of sunlight to reduce the thermal convection (Fig. 3e). To evaluate the cooling ability of the BDSS film, commercially available cooling fabric and white paper were selected as controls. We examined the time-dependent temperatures of the BDSS film (T_{BDSS}), flat film (T_{flat}), commercial cooling fabric ($T_{commercial}$), white paper (T_{white}), and the air (T_{air}) shielded with PE film (Fig. 3f) under continuous direct sunlight with an average power of 850 W m^{-2} (Fig. 3g) and relative humidity RH of 30–40% (Fig. 3h). The solar spectrum reflectivity and mid-infrared emissivity of white paper and the commercial cooling film are shown in Fig. S12 (ESI†). It is clear that the BDSS film achieves a lowest average temperature of ~40.2 °C, about 10.8 °C lower than T_{air}, 5.3 °C lower than $T_{commercial}$, and 3.7 °C lower than T_{white}, manifesting an excellent net cooling power of 94.67 W m^{-2} (Fig. S13, ESI†). More

importantly, the T_{BDSS} is 5.0 °C lower than T_{flat} on average (Fig. 3i), demonstrating an enhanced dual-scale structure effect on radiative cooling.

To verify the actual object cooling performance of the BDSS film, we placed the target film on the black cushion of a shared electric bicycle, which was directly exposed to sunlight from 11:50 to 12:50 (Fig. 4a). During the experiment, bicycle sunscreen seat material was used as a control to evaluate the cooling capability of the BDSS film. The infrared image shows that the BDSS film has an excellent cooling effect with a temperature reduction of 4.29 °C compared with the bicycle sunscreen seat material (Fig. 4b). A further time-dependent temperature monitoring shows that the cushion covered with BDSS film manifests an average temperature reduction of 14.0 °C compared with the bare cushion and 3.2 °C compared with the bicycle sunscreen seat material (Fig. 4c), which provides a practical method to cool the bicycle cushion in the hot summer. Fig. 4d–f shows the ability of the BDSS film to delay ice melting. Three 20 g ice cubes were placed in a self-made temperature measuring device. One of the ice cubes was kept bare, and the other two ice cubes were placed below the BDSS film and white paper (Fig. 4d). It was found that the cover of BDSS film can effectively delay the melting of the ice by regularly observing the intuitive shape and weight of the ice. This result is underpinned by the minimal rate of ice melting and water evaporation attributed to the excellent PRC performance and strong sunlight shading effect of the BDSS film. Taken together, our designed BDSS film exhibits excellent outdoor cooling capacity, which has potential applications in the thermal management of outdoor equipment.

Durability of the BDSS films

To verify the durability of the BDSS film, we implemented experiments to measure the self-cleaning, anti-corrosion of acid and alkali, flexibility, and anti-UV radiation performance of the BDSS film. We first examined the self-cleaning performance. Based on the enhancement of the dual-scale structure, the BDSS film shows superhydrophobicity with a water contact angle (CA) of 161° that is observed along the direction of the triangular ridge structure, in contrast to CA of ~119° on the flat film (Fig. 5a). Based on this, the BDSS film shows robust self-cleaning performance in that the deposited soil can be taken away by dripping water droplets in 8 s with no residue of soil and water (Fig. 5b). To verify the anti-corrosion of acid and alkali, we immersed the BDSS films into solutions with pH values ranging from 1 to 13 for 2 hours. The result shows that

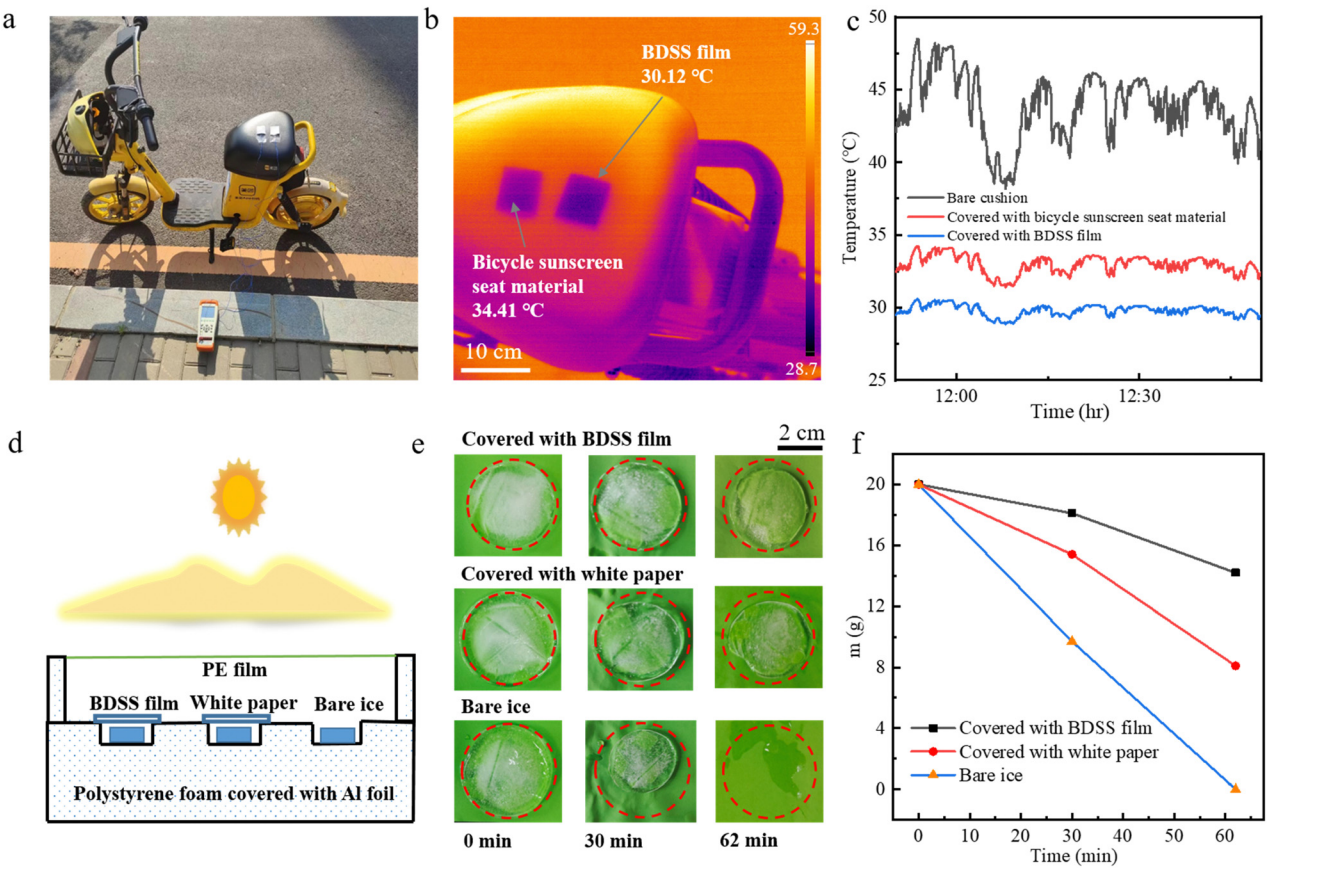

Fig. 4 BDSS film cooling test of actual objects. (a) Device for the cooling test of the shared electric bicycle cushion. (b) The infrared image presenting the cushion from left to right: the cushion covered with bicycle sunscreen seat material, the exposed cushion, and the cushion covered with the BDSS film. (c) The temperature curve of the cushion. (d) The schematic diagram of the device for icing delay. (e) The change of the volume and shape of ice with time. (f) The mass change curve of the ice cubes.

the surfaces still maintain superhydrophobicity with CA larger than 150° (Fig. 5c), demonstrating a robust performance for anti-corrosion of acid and alkali, which is mainly attributed to the isolation by an air cushion trapped at the solid–liquid interface.[48]

In addition, the BDSS film possesses excellent flexibility, and can recover to its original shape and superhydrophobic performance after being subjected to any stretching and twisting (Fig. 5d, e and Video S1, ESI†), ensuring a good fitting capacity for multi-shaped objects. A further tensile test shows that the SIRC film exhibited a strain tolerance of ~50% and yield limit of ~4 MPa, which are 5 times and 1.5 times those for the compared film prepared through phase separation (Fig. 5f),[49] indicating an excellent mechanical strength. More importantly, the optical properties of solar spectrum reflectivity and mid-infrared emissivity as well as the cooling capacity of BDSS film manifest robust stability comparable to those of the initial state after being treated with corrosion of acid (PH = 1) and alkali (PH = 13) in 120 h, exposure outdoor for 1 month, and stretching and twisting for 300 times (Fig. 5g and h). All these results indicate the robust durability of the BDSS film for working in specific extreme conditions.

Conclusions

In summary, we have for the first time discovered the excellent passive radiative cooling capacity of the inner surface of *Hawaiian scallop* shells underpinned by the dual-scale structure and proposed an ingenious method for bionic design and fabrication. The designed BDSS film possesses a solar spectrum reflectivity of 0.95 due to the enhanced Mie scattering by small-scale (~1 μm) steps and a mid-infrared emissivity of 0.98 by lengthening the propagation of photons induced by large-scale (~10 μm) triangular ridges. These excellent optical performances of BDSS film led to a sub-ambient cooling of 10.8 °C under direct sunlight. Moreover, the designed films manifest robust durability in various harsh scenarios endowed by outstanding self-cleaning, anti-corrosion of acid and alkali, flexibility, mechanical strength, and anti-UV radiation performances. The efficient passive radiative cooling accompanied by the robust durability of the BDSS films will offer promising potential in thermal management settings.

Experimental section

Materials

Shells (The shells used in this work are all from *Hawaiian scallops*) were purchased from the local seafood market in Dalian (Dalian, China). Polydimethylsiloxane (PDMS, Sylgard 184 Silicone Elastomer Kit with components of PDMS elastomer precursor base A and curing agent B) was purchased from Dow Corning (Michigan, America). Al_2O_3 particles were purchased from Hebei Qinghe County Science and Metallurgical Materials Co., Ltd (Qinghe, China). Polyethylene film (PE film), aluminum foil, and polystyrene foam were purchased from a local market. All chemicals were used without further purification.

Fabrication of BDSS films

Initially, a template for the BDSS film was created using a silicon wafer. The fabrication of the silicon wafer template involves lithography and etching processes. In the lithography process, the first step was fabricating the mask *via* a quartz glass plate with a certain shape. The glass was coated with an opaque layer of chrome. Certain areas of chrome were then removed according to the design, leaving transparent glass where light could pass through. The second step was cleaning the silicon wafer (with a size of 6 inches and thickness of 500 μm) to remove the dust, oil stains, and various organic and inorganic pollutants to ensure a high cleanliness degree of the surface. The third step was spin-coating, where a photoresist was applied evenly to the silicon wafer with a 100 nm thick layer of silicon nitride (Si_3N_4) on top. After that, a reactive ion etching was performed to remove the exposed Si_3N_4 and release the silicon substrate after the pattern transferred from the photomask to the photoresist. Then a wet etching stage was carried out. The etchant, etching temperature, and etching time were $KOH:H_2O$ at a ratio of 100 : 86, 85 °C, and three minutes. After etching, the silicon wafer was cleaned to get rid of any leftover photoresist and silicon nitride. Finally, a hydrophobic C_4F_8 thin film was deposited on the template to facilitate the demolding process.

After the fabrication of the wafer template, a mixture of Al_2O_3 particles and PDMS (ratio of precursors and curing agents is 10 : 1) in a certain proportion was covered on the wafer template *via* a spin-coating method. The coating speed and time could be adjusted to manage the film thickness. Then, the template coated with the mixture was placed in a vacuum oven, vacuumed for two hours, and then heated for two hours at 80 °C. Finally, the cured film was peeled off from the silicon wafer template to obtain a BDSS film.

Characterization

Field emission scanning electron microscopy (SU5000, Hitachi, Japan) was used to characterize the microscopic structure of the scallop and BDSS films. To measure the reflectivity in the solar spectrum (0.25–2.5 μm), a UV/Vis/NIR spectrophotometer with an integrating sphere (Lambda 950, PerkinElmer, America) was employed. A mid/near-infrared integrating sphere (VERTEX 70, BRUKER, America) was utilized in an FTIR spectrometer to measure the reflectivity between 7 and 15 μm. A single-lens reflex camera (EOS 5D MarkIV, Cannon, Japan) was used to capture the optical images. A contact angle meter (OCA25, Dataphysics GmbH, Germany) was used to measure the water contact angles on the designed surface. The volume of the water droplet was 3 μL and the water contact angle was calculated by averaging five readings. The surface temperature was measured using an infrared camera (Fotric-288, Fotric, China).

Outdoor passive radiative cooling performance measurement

To evaluate the outdoor PRC performance, a homemade cooling experimental setup was created and constructed. The subject of the setup was polystyrene foam (35 cm × 20 cm × 10 cm in length, width, and height) with five cavities (3 cm × 3 cm × 1 cm).

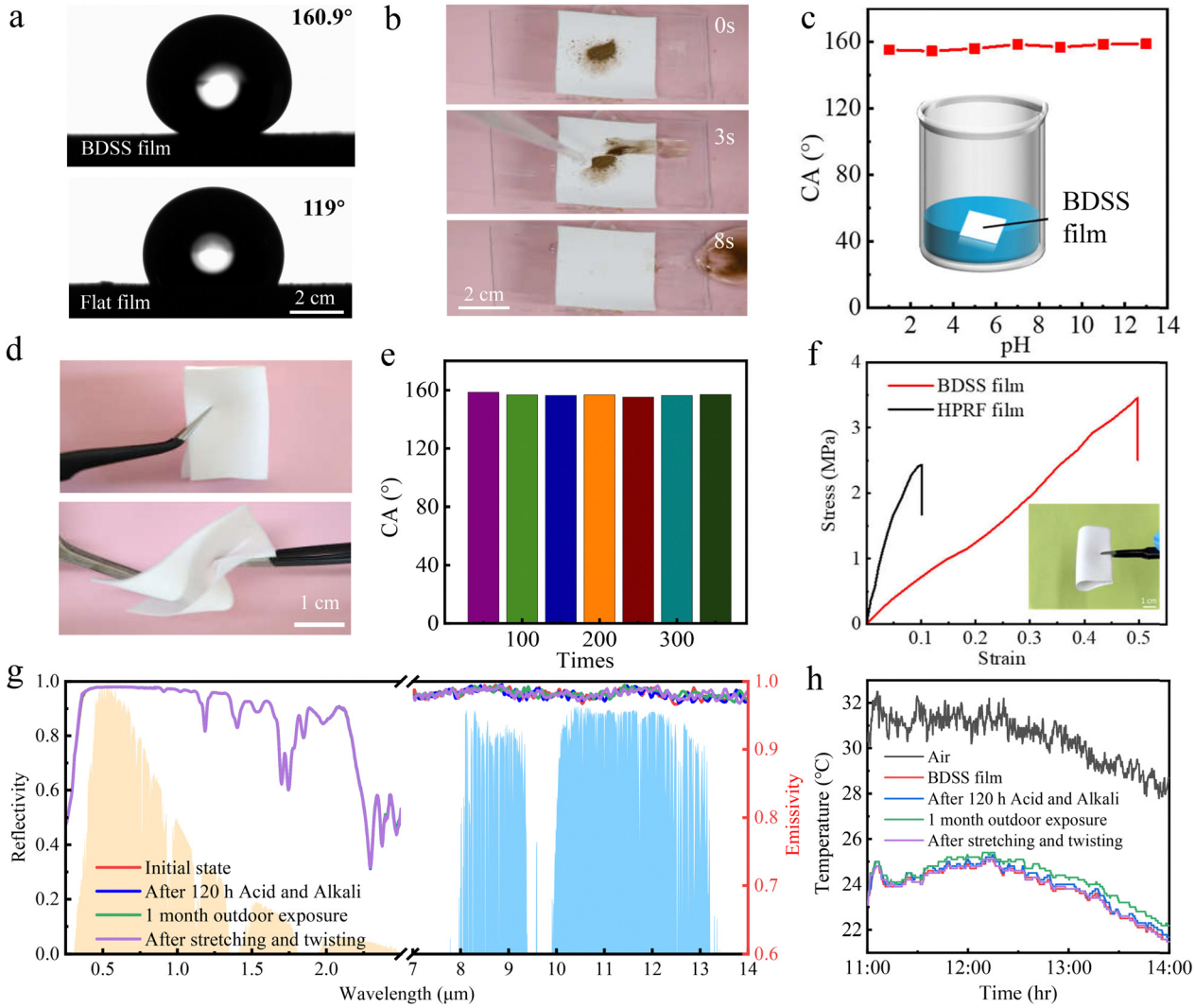

Fig. 5 Durability of the BDSS film. (a) Contact angle (CA) of the film that is observed along the direction of the triangular ridge structure. (b) The self-cleaning experiments of the surface. (c) CA of the BDSS film immersed in different pH solutions for 120 h. (d) Bending and torsion experiment of the BDSS film. (e) CA of the BDSS film with different times of stretching and torsion. (f) The tensile tests of the BDSS film and the controlled film prepared by the phase separation method. (g) Optical properties of the BDSS film after 120 h chemical durability, ultraviolet exposure, and bending torsion. (h) Cooling test of the BDSS film after 120 h chemical durability, ultraviolet exposure, and bending torsion.

In addition, the polystyrene foam was sealed with a PE film that has high transparency for both sunlight and infrared light and wrapped with aluminum foil that could reflect light well. In our experiment, we filled four of the cavities with BDSS film, flat film, commercial cooling fabric, and whitepaper. Then we tested the temperature inside each cavity by placing the K-type thermocouple sensor into each of the recesses by using an eight-channel multi-temperature logger (JK-808, JINKO, China). Furthermore, a sun photometer (TES-132, TES, China), and a humidity logger (TH20E, ANYMETRE, China) were employed to measure the solar power and relative humidity, respectively.

Calculation of the solar spectrum reflectivity and mid-infrared emissivity

Maximizing reflectivity in the solar spectrum band (0.25–2.5 μm) and emissivity in the atmospheric window region (8–13 μm) are essential for achieving PRC during daytime. The calculation formulas of the solar spectrum reflectivity ($\bar{R}_{\mathrm{solar}}$) and thermal emissivity ($\bar{E}_{\mathrm{TIR}}$) are as follows:

$$\bar{R}_{\mathrm{solar}} = \frac{\int_{280\mathrm{nm}}^{2500\mathrm{nm}} I_{\mathrm{sun}}(\lambda) R_{\mathrm{sun}}(\lambda) \mathrm{d}\lambda}{\int_{280\mathrm{nm}}^{2500\mathrm{nm}} I_{\mathrm{sun}}(\lambda) \mathrm{d}\lambda} \quad (1)$$

Here, 280–2500 nm is the solar spectrum. λ is the wavelength. $I_{\mathrm{sun}}(\lambda)$ is the Air Mass 1.5 global solar spectrum. $R_{\mathrm{sun}}(\lambda)$ is the reflectivity of the sample.

$$\bar{E}_{\mathrm{MIR}} = \frac{\int_{8\mu\mathrm{m}}^{13\mu\mathrm{m}} I_{\mathrm{B}}(\lambda, T)(1 - R_{\mathrm{MIR}}(\lambda)) \mathrm{d}\lambda}{\int_{8\mu\mathrm{m}}^{13\mu\mathrm{m}} I_{\mathrm{B}}(\lambda, T) \mathrm{d}\lambda} \quad (2)$$

$$I_B(\lambda, T) = \frac{2hc^2}{\lambda^5\left(e^{\frac{hc}{K_B T}} - 1\right)} \quad (3)$$

Here, 8–13 μm is the atmospheric window, $R_{MIR}(\lambda)$ is the reflectivity of the sample. According to Kirchhoff's law of thermal radiation, under the premise of ignoring the transmittance, the emissivity is obtained by measuring the reflectivity $R_{MIR}(\lambda)$. $I_B(\lambda,T)$ is the blackbody radiation at temperature T. c is the speed of light, h is Planck's constant, and K_B is Boltzmann's constant.

Calculation of cooling power

At temperature T, consider a radiative cooler of area A whose spectral and angular emissivity is $\epsilon(\lambda, \theta)$. The radiative cooler is exposed to both solar radiation and atmospheric thermal radiation (which corresponds to the ambient air temperature T_{amb}) when it is in the daytime. For such a radiative cooler, the net cooling power P_{net} is provided by:

$$P_{net}(T) = P_{rad}(T) - P_{atm}(T_{atm}) - P_{solar} - P_{cond+conv} \quad (4)$$

$$P_{rad}(T) = A\int d\Omega \cos\theta \int_0^\infty d\lambda I_{BB}(T, \lambda)\epsilon(\lambda, \theta) \quad (5)$$

Here $\int d\Omega = 2\pi\int_0^{\pi/2} d\theta \sin\theta$ is the hemispheric angular integral. $I_{BB}(T, \lambda) = \frac{2hc^2}{\lambda^5}\frac{1}{e^{hc/(\lambda k_B T)} - 1}$ is the blackbody's spectral brightness at a temperature T, where λ is the wavelength, c is the speed of light, h is Planck's constant, and k_B is the Boltzmann constant.

$$P_{atm}(T_{atm}) = A\int d\Omega \cos\theta \int_0^\infty d\lambda I_{BB}(T_{amb}, \lambda)\epsilon(\lambda, \theta)\epsilon_{atm}(\lambda, \theta) \quad (6)$$

$$P_{solar} = A\int_0^\infty d\lambda \epsilon(\lambda, \theta_{solar}) I_{AM1.5}(\lambda) \quad (7)$$

Here $I_{AM1.5}(\lambda)$ is spectral irradiance intensity calculated based on the AM1.5 standard solar spectrum.

$$P_{cond+conv}(T, T_{amb}) = Ah_c(T_{amb} - T) \quad (8)$$

Here $h_c = h_{cond} + h_{conv}$ is a combined non-radiative heat coefficient that accounts for the combined impact of convective and conductive heating caused by the radiative cooler's contact with the surrounding air and exterior surfaces.

Author contributions

R. Z. proposed the initial idea; R. Z. and S. F. designed the experiment and analyzed the results; R. Z. and S. W. performed the experiments. S. F., Y. L., L. Z., N. S., and M. Z. supervised the project and provided critical suggestions. R. Z., and S. F. drafted the manuscript, and all authors revised the manuscript.

Conflicts of interest

There are no conflicts to declare.

Acknowledgements

The work was supported by the National High-Level Talents Special Support Program, the Outstanding Youth Natural Science Foundation of Liaoning Province (2022-YQ-11), the Liao Ning Revitalization Talents Program (XLYC2203049), the National Natural Science Foundation of China (52005075), and the Dalian Youth Science and Technology Star Project.

References

1 M. Panteli and P. Mancarella, *Electr. Power Syst. Res.*, 2015, **127**, 259–270.
2 C. Lesk, P. Rowhani and N. Ramankutty, *Nature*, 2016, **529**, 84.
3 D. Tong, Q. Zhang, Y. Zheng, K. Caldeira, C. Shearer, C. Hong, Y. Qin and S. J. Davis, *Nature*, 2019, **572**, 373.
4 S. Atiganyanun, J. B. Plumley, S. J. Han, K. Hsu, J. Cytrynbaum, T. L. Peng, S. M. Han and S. E. Han, *ACS Photonics*, 2018, **5**, 1181–1187.
5 B. Bhatia, A. Leroy, Y. Shen, L. Zhao, M. Gianello, D. Li, T. Gu, J. Hu, M. Soljacic and E. N. Wang, *Nat. Commun.*, 2018, **9**, 5001.
6 L. Cai, A. Y. Song, W. Li, P.-C. Hsu, D. Lin, P. B. Catrysse, Y. Liu, Y. Peng, J. Chen, H. Wang, J. Xu, A. Yang, S. Fan and Y. Cui, *Adv. Mater.*, 2018, **30**, 1802152.
7 M. Ono, K. Chen, W. Li and S. Fan, *Opt. Express*, 2018, **26**, A777–A787.
8 A. Leroy, B. Bhatia, C. C. Kelsall, A. Castillejo-Cuberos, M. H. Di Capua, L. Zhao, L. Zhang, A. M. Guzman and E. N. Wang, *Sci. Adv.*, 2019, **5**, eaat9480.
9 E. Rephaeli, A. Raman and S. Fan, *Nano Lett.*, 2013, **13**, 1457–1461.
10 L. Zhu, A. Raman, K. X. Wang, M. Abou Anoma and S. Fan, *Optica*, 2014, **1**, 32–38.
11 M. M. Hossain, B. Jia and M. Gu, *Adv. Opt. Mater.*, 2015, **3**, 1047–1051.
12 L. Zhu, A. P. Raman and S. Fan, *Proc. Natl. Acad. Sci. U. S. A.*, 2015, **112**, 12282–12287.
13 M. M. Hossain and M. Gu, *Adv. Sci.*, 2016, **3**, 1500360.
14 H. Bao, C. Yan, B. Wang, X. Fang, C. Y. Zhao and X. Ruan, *Sol. Energy Mater. Sol. Cells*, 2017, **168**, 78–84.
15 T. Li, Y. Zhai, S. He, W. Gan, Z. Wei, M. Heidarinejad, D. Dalgo, R. Mi, X. Zhao, J. Song, J. Dai, C. Chen, A. Aili, A. Vellore, A. Martini, R. Yang, J. Srebric, X. Yin and L. Hu, *Science*, 2019, **364**, 760.
16 D. Rosenfeld, Y. Zhu, M. Wang, Y. Zheng, T. Goren and S. Yu, *Science*, 2019, **363**, 599.
17 D. Zhao, A. Aili, Y. Zhai, J. Lu, D. Kidd, G. Tan, X. Yin and R. Yang, *Joule*, 2019, **3**, 111–123.
18 D. Chae, M. Kim, P.-H. Jung, S. Son, J. Seo, Y. Liu, B. J. Lee and H. Lee, *ACS Appl. Mater. Interfaces*, 2020, **12**, 8073–8081.
19 S.-Y. Heo, G. J. Lee, H. Kim, Y. J. Kim, S. Ishii, M. S. Kim, T. J. Seok, B. J. Lee, H. Lee and Y. M. Song, *Sci. Adv.*, 2020, **6**, eaab1906.
20 X. Wang, X. Liu, Z. Li, H. Zhang, Z. Yang, H. Zhou and T. Fan, *Adv. Funct. Mater.*, 2020, **30**, 1907562.

21 X. Xue, M. Qiu, Y. Li, Q. M. Zhang, S. Li, Z. Yang, C. Feng, W. Zhang, J.-G. Dai, D. Lei, W. Jin, L. Xu, T. Zhang, J. Qin, H. Wang and S. Fan, *Adv. Mater.*, 2020, **32**, 1906751.
22 D. Li, X. Liu, W. Li, Z. Lin, B. Zhu, Z. Li, J. Li, B. Li, S. Fan, J. Xie and J. Zhu, *Nat. Nanotechnol.*, 2021, **16**, 153.
23 X. Li, J. Peoples, P. Yao and X. Ruan, *ACS Appl. Mater. Interfaces*, 2021, **13**, 21733–21739.
24 K. Tang, K. Dong, J. Li, M. P. Gordon, F. G. Reichertz, H. Kim, Y. Rho, Q. Wang, C.-Y. Lin, C. P. Grigoropoulos, A. Javey, J. J. Urban, J. Yao, R. Levinson and J. Wu, *Science*, 2021, **374**, 1504.
25 S. Wang, T. Jiang, Y. Meng, R. Yang, G. Tan and Y. Long, *Science*, 2021, **374**, 1501.
26 T. Wang, Y. Wu, L. Shi, X. Hu, M. Chen and L. Wu, *Nat. Commun.*, 2021, **12**, 365.
27 B. Xiang, R. Zhang, Y. Luo, S. Zhang, L. Xu, H. Min, S. Tang and X. Meng, *Nano Energy*, 2021, **81**, 105600.
28 A. P. Raman, M. Abou Anoma, L. Zhu, E. Rephaeli and S. Fan, *Nature*, 2014, **515**, 540.
29 C. Zou, G. Ren, M. M. Hossain, S. Nirantar, W. Withayachumnankul, T. Ahmed, M. Bhaskaran, S. Sriram, M. Gu and C. Fumeaux, *Adv. Opt. Mater.*, 2017, **5**, 1700460.
30 S. Zeng, S. Pian, M. Su, Z. Wang, M. Wu, X. Liu, M. Chen, Y. Xiang, J. Wu, M. Zhang, Q. Cen, Y. Tang, X. Zhou, Z. Huang, R. Wang, A. Tunuhe, X. Sun, Z. Xia, M. Tian, M. Chen, X. Ma, L. Yang, J. Zhou, H. Zhou, Q. Yang, X. Li, Y. Ma and G. Tao, *Science*, 2021, **373**, 692.
31 M. Zhou, H. Song, X. Xu, A. Shahsafi, Y. Qu, Z. Xia, Z. Ma, M. A. Kats, J. Zhu, B. S. Ooi, Q. Gan and Z. Yu, *Proc. Natl. Acad. Sci. U. S. A.*, 2021, **118**, 2019292118.
32 B. Zhu, W. Li, Q. Zhang, D. Li, X. Liu, Y. Wang, N. Xu, Z. Wu, J. Li, X. Li, P. B. Catrysse, W. Xu, S. Fan and J. Zhu, *Nat. Nanotechnol.*, 2021, **16**, 1342–U1336.
33 J. Jaramillo-Fernandez, H. Yang, L. Schertel, G. L. Whitworth, P. D. Garcia, S. Vignolini and C. M. Sotomayor-Torres, *Adv. Sci.*, 2022, **9**, 2104758.
34 S. H. Choi, S.-W. Kim, Z. Ku, M. A. Visbal-Onufrak, S.-R. Kim, K.-H. Choi, H. Ko, W. Choi, A. M. Urbas, T.-W. Goo and Y. L. Kim, *Nat. Commun.*, 2018, **9**, 452.
35 A. Krishna, X. Nie, A. D. Warren, J. E. Llorente-Bousquets, A. D. Briscoe and J. Lee, *Proc. Natl. Acad. Sci. U. S. A.*, 2020, **117**, 1566–1572.
36 X. Liu, D. Wang, Z. Yang, H. Zhou, Q. Zhao and T. Fan, *Adv. Opt. Mater.*, 2019, **7**, 1900687.
37 C. Lou, S. An, R. Yang, H. Zhu, Q. Shen, M. Jiang, B. Fu, P. Tao, C. Song, T. Deng and W. Shang, *Apl Photonics*, 2021, **6**, 036101.
38 I. Medina, E. Newton, M. R. Kearney, R. A. Mulder, W. P. Porter and D. Stuart-Fox, *Nat. Commun.*, 2018, **9**, 3610.
39 C.-C. Tsai, R. A. Childers, N. N. Shi, C. Ren, J. N. Pelaez, G. D. Bernard, N. E. Pierce and N. Yu, *Nat. Commun.*, 2020, **11**, 551.
40 Z. Yang, H. Sun, Y. Xi, Y. Qi, Z. Mao, P. Wang and J. Zhang, *Sol. Energy Mater. Sol. Cells*, 2021, **227**, 111101.
41 H. Zhang, K. C. S. Ly, X. Liu, Z. Chen, M. Yan, Z. Wu, X. Wang, Y. Zheng, H. Zhou and T. Fan, *Proc. Natl. Acad. Sci. U. S. A.*, 2020, **117**, 14657–14666.
42 N. N. Shi, C.-C. Tsai, F. Camino, G. D. Bernard, N. Yu and R. Wehner, *Science*, 2015, **349**, 298–301.
43 D. Xie, Z. Yang, X. Liu, S. Cui, H. Zhou and T. Fan, *Soft Matter*, 2019, **15**, 4294–4300.
44 N. N. Shi, C.-C. Tsai, M. J. Carter, J. Mandal, A. C. Overvig, M. Y. Sfeir, M. Lu, C. L. Craig, G. D. Bernard, Y. Yang and N. Yu, *Light: Sci. Appl.*, 2018, **7**, 37.
45 L. Xiong, Y. Wei, C. Chen, X. Chen, Q. Fu and H. Deng, *Nat. Commun.*, 2023, **14**, 6129.
46 Z. Cheng, H. Han, F. Wang, Y. Yan, X. Shi, H. Liang, X. Zhang and Y. Shuai, *Nano Energy*, 2021, **89**, 106377.
47 J. Mandal, Y. Fu, A. C. Overvig, M. Jia, K. Sun, N. N. Shi, H. Zhou, X. Xiao, N. Yu and Y. Yang, *Science*, 2018, **362**, 315–318.
48 M.-C. Huang, C.-H. Xue, J. Huang, B.-Y. Liu, X.-J. Guo, Z.-X. Bai, R.-X. Wei, H.-D. Wang, M.-M. Du, S.-T. Jia, Z. Chen and Y. Lai, *Chem. Eng. J.*, 2022, **442**, 136239.
49 L. Zhang, H. Zhan, Y. Xia, R. Zhang, J. Xue, J. Yong, L. Zhao, Y. Liu and S. Feng, *ACS Appl. Mater. Interfaces*, 2023, **15**, 31994–32001.